

Boundary Layer Ingestion Benefit of the D8 Transport Aircraft

Alejandra Uranga*

University of Southern California, Los Angeles, California 90089

Mark Drela,[†] Edward M. Greitzer,[‡] David K. Hall,[§] Neil A. Titchener,^{||} Michael K. Lieu,^{**}

Nina M. Siu,^{**} Cécile Casses,^{**} and Arthur C. Huang^{††}

Massachusetts Institute of Technology, Cambridge, Massachusetts 02139

and

Gregory M. Gatlin^{‡‡} and Judith A. Hannon^{§§}

NASA Langley Research Center, Hampton, Virginia 23681

DOI: 10.2514/1.J055755

This paper presents the experimental assessment of the aerodynamic benefit of boundary layer ingestion for an advanced design civil transport aircraft, the D8 “double bubble,” carried out from 2010 to 2015 as part of a NASA N + 3 Phase 2 Program. A back-to-back comparison of non-boundary layer ingesting and boundary layer ingesting versions of the D8 was conducted using 1:11-scale powered models in the NASA Langley 14- by 22-foot subsonic tunnel. The aerodynamic benefit of boundary layer ingestion, as quantified by the difference in mechanical flow power required with boundary layer ingestion relative to the non-boundary layer ingesting case, was measured using two different methods to be 8.6% at the simulated cruise condition when the same propulsors are used on the two configurations. The benefit is found to be insensitive to the various modeling and processing assumptions. A detailed error analysis shows that the benefit has an uncertainty fraction of 0.21 and a 95% confidence interval fraction of 0.035, thus giving high confidence to these results. This work represents the first measurement of boundary layer ingestion performance improvements for a realistic civil aircraft configuration and provides a proof-of-concept for the use of boundary layer ingestion to improve fuel efficiency of subsonic transports.

Nomenclature

A_{fan}	= fan area (excludes hub area), equal to 24.64 in. ² (0.0159 m ²)
A_{nozzle}	= exit nozzle area
\mathcal{R}	= aspect ratio, equal to a span ² / S_{ref} of 15.43
C_D	= drag coefficient
C_L	= vertical aerodynamic force (lift) coefficient, equal to $F_Z/(q_\infty S_{\text{ref}})$
C_m	= pitching moment coefficient, equal to $M_Y/(q_\infty S_{\text{ref}} c)$
C_n	= yawing moment coefficient, equal to $M_Z/(q_\infty S_{\text{ref}} c)$
C_{P_E}	= electrical power coefficient, equal to $P_E/(q_\infty V_\infty S_{\text{ref}})$
C_{P_K}	= mechanical flow power coefficient, equal to $P_K/(q_\infty V_\infty S_{\text{ref}})$
C_X	= net streamwise force coefficient, equal to $F_X/(q_\infty S_{\text{ref}})$
C_Φ	= dissipation coefficient, equal to $\Phi/(q_\infty V_\infty S_{\text{ref}})$

c	= model reference chord, equal to 10.75 in. (0.273 m)
d_{fan}	= model propulsor fan diameter, equal to 5.65 in. (0.144 m)
e	= span efficiency
F_X	= net streamwise force; $F_X < 0$ indicates net thrust
F_Z	= vertical aerodynamic force (lift) on model, in Z direction
M_Y	= pitching moment
M_Z	= yawing moment
M_∞	= freestream (tunnel) Mach number
\hat{n}	= unit normal vector
PSC	= power saving coefficient, equal to $(P'_K - P_K)/P'_K$
P_E	= electrical power supplied to propulsors
P_K	= mechanical flow power
P_{Shaft}	= propulsor shaft power
P_V	= volumetric flow power
p	= static pressure
p_t	= total pressure
p_{t_∞}	= freestream (tunnel) total pressure
p_∞	= freestream (tunnel) static pressure
q_∞	= freestream (tunnel) dynamic pressure, equal to $1/2\rho_\infty V_\infty^2$
Re_c	= reference-chord Reynolds number, equal to $\rho_\infty V_\infty c/\mu_\infty$
S	= surface of body, including propulsor inlet and outlet surfaces
S_{ref}	= model reference area, equal to 1686 in. ² (1.088 m ²)
U_{tip}	= fan blade tip speed, equal to $\Omega d_{\text{fan}}/2$
V	= velocity magnitude (speed), equal to $ V $
\mathbf{V}	= velocity vector
\mathcal{V}	= fluid control volume surrounding body
V_{fan}	= average velocity at the fan face in the fan axial direction
V_∞	= freestream (tunnel) speed
X, Y, Z	= tunnel axes, where X is streamwise, Z is vertical
α	= model angle of attack
$\Delta()$	= data correction quantity
η_f	= fan efficiency, equal to P_K/P_{Shaft}
η_m	= motor efficiency, equal to P_{Shaft}/P_E

Received 28 November 2016; revision received 2 May 2017; accepted for publication 26 May 2017; published online Open Access 24 August 2017. Copyright © 2017 by A. Uranga, M. Drela, and E. M. Greitzer. Published by the American Institute of Aeronautics and Astronautics, Inc., with permission. All requests for copying and permission to reprint should be submitted to CCC at www.copyright.com; employ the ISSN 0001-1452 (print) or 1533-385X (online) to initiate your request. See also AIAA Rights and Permissions www.aiaa.org/randp.

*Assistant Professor, Department of Aerospace and Mechanical Engineering, 854 Downey Way RRB218; former Research Engineer in Massachusetts Institute of Technology's Department of Aeronautics and Astronautics; auranga@usc.edu. Senior Member AIAA.

[†]Terry J. Kohler Professor of Fluid Dynamics, Department of Aeronautics and Astronautics. Fellow AIAA.

[‡]H.N. Slater Professor of Aeronautics and Astronautics. Honorary Fellow AIAA.

[§]Postdoctoral Associate. Member AIAA.

^{||}Former Postdoctoral Associate in Aeronautics and Astronautics.

^{**}Former Graduate Student in Aeronautics and Astronautics.

^{††}Graduate Student in Aeronautics and Astronautics.

^{‡‡}Senior Research Engineer, Configuration Aerodynamics Branch, Mail Stop 267. Associate Fellow AIAA.

^{§§}Aerospace Engineer, Flow Physics and Control Branch, Mail Stop 170.

η_o	=	overall efficiency, equal to $\eta_m\eta_f$
ρ	=	fluid density
ρ_∞	=	freestream (tunnel) density
$\bar{\tau}$	=	viscous stress tensor
Φ	=	dissipation
Φ_∞	=	total viscous dissipation in flowfield
ϕ	=	flow coefficient, equal to V_{fan}/U_{tip}
Ω	=	propulsor fan angular velocity or wheel speed

Subscripts

LaRC	=	NASA Langley Research Center 14- by 22-foot subsonic-tunnel quantity
MIT	=	Massachusetts Institute of Technology 1 × 1 ft wind-tunnel quantity

Superscript

'	=	quantity for non-boundary layer ingesting configuration
---	---	---

I. Introduction

A. Motivation

AIRLINE traffic has seen a steady increase through the last 40 years and is projected to maintain a close to 5% growth for the next 20 years [1–3]. As a result, there is an increased emphasis on reducing fuel burn and emissions of commercial aircraft, and meeting the targeted efficiency goals cannot be achieved solely from advancements in technology, operations, and infrastructure [4,5]. As a step in the quest for new improvements, this paper describes an experimental assessment of a conceptual clean-sheet redesign for commercial airliners, which shows the benefit that can be achieved by more closely integrating together the propulsion system and the airframe.

B. Boundary Layer Ingestion for Improving Fuel Efficiency

Several concepts for future aircraft have been proposed that use boundary layer ingestion (BLI) as a way to reach fuel efficiency levels not achievable with the conventional tube-and-wing design of current civil transport aircraft. Examples are the blended (or hybrid) wing bodies [6,7], configurations with distributed propulsion systems [8,9], and the D8 [10–12].

With BLI, a portion of the airframe's boundary layer is ingested and reenergized by the propulsors. Its theoretical benefit on propulsive efficiency is well established: BLI reduces the overall power dissipation in the flowfield [13], primarily by reducing wasted kinetic energy in the exhaust jet and also by "filling-in" the wake defect, as illustrated in Fig. 1.

A basic explanation given by Betz [14] is that reduced inflow velocity of the propulsive stream-tube results in less power being required to impart a given momentum. This idea was quantified by Smith [15], whose analysis for an unducted propulsor suggested that power savings as large as 50% were possible for some combinations of inflow wake profiles and high propeller disk loadings. For more practical cases, the savings were estimated to be 10–20%.

There have also been studies of simplified BLI configurations (e.g., a propulsor in the wake of an axisymmetric body) [16]. These provide validation data for numerical simulations and show good agreement with theoretical predictions, but the complexity of a BLI propulsor that is actually integrated in an airframe is not addressed.

The benefit of BLI might be reduced by the unfavorable effects of the distorted propulsor inflow on fan performance. The work by NASA and United Technologies Research Center to design a fan for transonic operation with BLI suggests that the fan-efficiency drop due to distortion can be kept to 1–3 percentage points [17,18] and there are possibilities for mitigating the negative effects of distortion [19].

One complication of BLI is the force accounting for the entire aircraft, because the usual notions of thrust and drag become ambiguous. An alternative approach based on the power balance framework of Drela [13] is employed here, because it is largely free of such ambiguities. Another complication arises when the merit of a

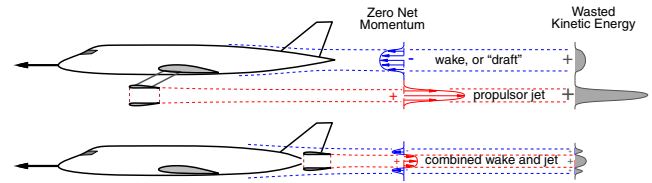


Fig. 1 Illustration of power-saving benefit of (bottom) boundary layer ingestion compared with (top) a conventional aircraft. Lower wake velocities of combined wake and jet result in a reduction in wasted kinetic energy.

propulsor employing BLI is to be evaluated, because the baseline propulsor without BLI is not uniquely defined [20]. The focus of the present paper is to evaluate the benefit gained from BLI when the same propulsor is used in conventional non-BLI and in BLI installations.

C. D8 Aircraft Concept

The aircraft configuration examined here is the D8 double bubble, named for its characteristic fuselage cross section. A 180 passenger, 3000 nm range transport in the Boeing 737 or Airbus A320 aircraft class, this Massachusetts Institute of Technology (MIT)-designed configuration is characterized by a wide twin-aisle lifting fuselage which enables the use of smaller, lighter wings and a pi-tail empennage with the horizontal tail supported by twin vertical tails. The fuselage nose shape provides a nose-up pitching moment that reduces the trimming tail downforce in cruise and further shrinks both the wing and horizontal tail areas. A low-sweep wing that contributes to a lighter structure is made possible by a cruise speed of Mach 0.72, compared with around Mach 0.78 for a conventional tube-and-wing aircraft in the same class [11]. Additional features that contribute to the fuel-burn reduction are described in [10–12]. (The choice of using a 737-class aircraft as the baseline was made during the N + 3 Phase 1 Project [10] based on analysis of the worldwide commercial aircraft fleet with the goal of maximizing the impact that a new aircraft could have. The term 737-800 is used, but at the level of details of our conceptual estimates, it also represents an A320.)

A major feature of the D8 configuration is that the engines are flush mounted on the top rear of the fuselage and ingest approximately 13% of the total airframe viscous dissipation^{††} (or roughly 40% of the fuselage boundary layer). The engines are located near the fuselage's rear stagnation point, and the fuselage performs much of the diffusion and flow alignment into the fans, which would otherwise be achieved by the nacelle. The D8 nacelles are thus smaller than for conventional podded engines, saving weight and reducing external losses. Boundary layer ingestion is an enabling technology for achieving the fuel efficiency levels of the D8 and is the focus of this work.

The D8.2 variant is studied here, which is a twin-engine aircraft^{***} that employs aluminum materials and whose shape is shown in Fig. 2. Compared with a conventional tube-and-wing aircraft, the D8.2 achieves a 36% reduction in fuel burn from the configuration alone (i.e., without advanced materials or engines). Additional technological advances expected to occur in the next 20–30 years, incorporated in the D8.6 concept, are estimated to have the potential to yield fuel burn savings close to 65% [21].

The geometry near the engines is complex and includes integration with the rear fuselage and the twin vertical tails, and so there is a possibility of interference losses. The geometric outer mold lines used in the present study (designed by Uranga and Drela in early 2013) represent a first attempt at the aerodynamic design of the installation. The wind-tunnel measurements indicate that this configuration can be realized with good aerodynamic performance. An engine architecture specifically tailored for the D8, and that addresses certification concerns for side-to-side engines, is discussed in [22].

^{††}BLI fractions are computed based on boundary layer kinetic energy defect.

^{***}The first D8 studies of phase 1 [10] employed three engines. Switching to two engines results in a slight performance decrease but addresses cost and maintenance concerns.

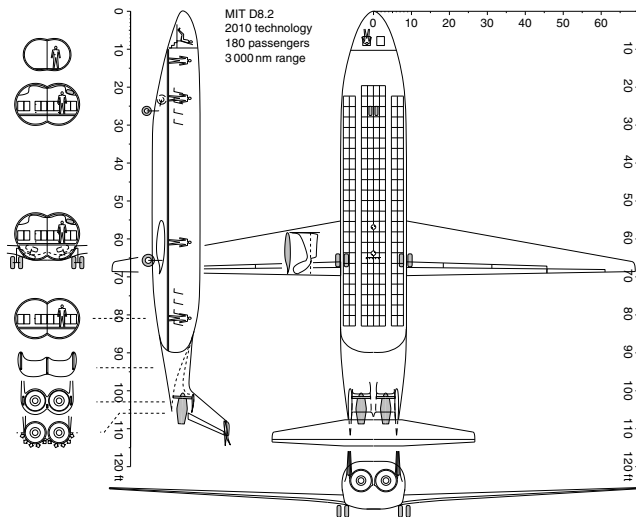


Fig. 2 Three-view of D8.2 transport aircraft concept.

D. NASA N + 3 Program

Recognizing the need for substantial improvements in aircraft performance, NASA put forward a solicitation in 2008 for aircraft concepts targeted for three generations ahead of the current fleet. This “N + 3” program aims to develop advanced concepts and enabling technologies, to provide step improvements in fuel efficiency of commercial aircraft entering service in the 2025–2035 timeframe. During phase 1 of the program (September 2008–March 2010, NASA–MIT cooperative agreement NNX08AW63A), a team led by MIT, in partnership with Aurora Flight Sciences and Pratt and Whitney, created a conceptual design for the D8, an aircraft that met the aggressive NASA goals [10].

Phase 2 of the program (November 2010–May 2015, NASA–MIT cooperative agreement NNX11AB35A) included the aerodynamic design of the integrated fuselage and propulsion system for the D8 and the development of scaling arguments, metrics, and baselines for evaluation of fuselage boundary layer ingestion as a way to reach higher fuel efficiency levels. A major component was a series of low-speed (roughly Mach 0.1) experiments in the NASA Langley 14- by 22-foot subsonic tunnel using a 1:11-scale, 4-m-span (13.4 ft) powered model (shown in Fig. 3) to compare the aerodynamic performance of the D8 with and without BLI. Preliminary results were presented by Uranga et al. after the first tunnel test campaign of 2013 [12]. A second campaign was undertaken in 2014 to obtain additional data and to reduce uncertainty in the measured BLI benefit. This paper presents the major findings of these experiments.

The main focus of the experiments was to determine the aerodynamic BLI benefit, defined as the change in mechanical flow power required to produce a given net streamwise force when going



Fig. 3 D8 model with BLI propulsors in NASA Langley's 14- by 22-foot subsonic tunnel during the 2013 tests (photo credit NASA/George Homich).

from a non-BLI to a BLI aircraft configuration. Of particular interest is the simulated cruise condition, because for medium- to long-haul flights about 80% of the mission fuel is burnt during cruise.

E. Paper Scope

This paper presents detailed measurements of the power reduction due to BLI for a realistic transport aircraft configuration model. As the first back-to-back comparison of BLI and non-BLI configurations, it is both a proof-of-concept for fuel burn reduction through the use of BLI and a data set to assess estimates in the conceptual design and analysis of novel transport aircraft. The benefits of BLI are evaluated as aerodynamic and propulsive-efficiency gains via the mechanical flow power, which is independent of propulsor-specific characteristics and only weakly dependent on installation details. Thus, the results of the present work constitute generic and realistic estimates of the benefits achievable with BLI for transport aircraft.

It must be stressed that the D8 wind-tunnel tests are not conventional propulsion tests. The goal was not to determine the propulsor performance (e.g., thrust) under different installations, but rather to evaluate the aircraft configuration overall performance, with the benefit of BLI simply determined by the power required to maintain flight.

In this context, the model is seen as a system whose components are interdependent. BLI tightly couples the propulsion system with the body (airframe), and it was a deliberate choice not to separate the force contributions from each of these subsystems. Decomposing the measured overall forces (without the gathering of additional experimental data in an additional test) would require introducing assumptions and approximations that are extraneous to the experimental measurements and the goal of the experiments and would therefore reduce, rather than strengthen, the value of the reported experimental results.

In this paper, the experimental results obtained with the same propulsor for both configurations are reported, which is a measure of the BLI benefit at equal nozzle area. Results obtained for a range of nozzle areas will be reported in another publication. More detailed descriptions of the wind-tunnel models, experimental procedures, and uncertainty and sensitivities results can be found in the project's Phase 2 Final Report [21].

Presented next is a brief analysis of BLI and performance metrics. A description of the non-BLI and BLI configurations of the D8 is then provided, followed by explanation of the methods used to compute the mechanical flow power and a description of the experiments. The results for the aerodynamic benefit of BLI are presented and the applicability of these low Mach number subscale results to full-size aircraft are then discussed. Finally, a summary and conclusions are provided.

II. Boundary Layer Ingestion Analysis

A. Power as Performance Metric

For BLI propulsors that are aerodynamically integrated with the airframe, conventional notions of drag and thrust become ambiguous. This is most obvious when the forces are defined in terms of surface pressure and shear forces, because the surface cannot be meaningfully subdivided into power plant and airframe portions. Ambiguity also appears when the forces are defined in terms of pressures and momentum flux changes on an outer control volume surface, because the streamtube passing through the propulsor has interacted with the airframe and thus carries both “thrust” and “drag” contributions. Only the total net streamwise, “drag minus thrust,” force remains well defined.

Historically, this problem has been approached by modifying the usual force bookkeeping terms such as airframe drag, ram drag, and gross thrust, by introducing quantities like “ingested drag,” “scrub drag,” etc. Typically, these quantities represent control volume analyses on partial volumes surrounding portions of the aircraft [23,24]. However, because the rest of the airframe is not also wrapped by similar control volumes in these procedures, the overall analysis is

not reducible to an overall momentum integral on an overall control surface surrounding the aircraft and there is no guarantee that these calculation procedures correctly give the net overall force on the aircraft.

An alternative approach based on the power balance framework [13] is employed here. Propulsive power was used previously by Smith [15] as the relevant metric for the merit of BLI, but he still assumed that the airframe's viscous flow and hence its drag is given. In the power balance framework applied here, the entire aerodynamic flowfield of the airframe plus propulsors is included in one analysis that unifies all the power losses on the aircraft. The surface boundary layer losses of the airframe and the propulsive losses of the power plant are related to the power (and hence fuel burn) of the propulsor, without the need for separate drag and thrust force estimates or the need to define a “reduced drag” or “increased thrust” in integrated configurations. The work of Sato [25] demonstrated the effectiveness of the power balance framework for estimating the aerodynamic characteristics of a variety of configurations with and without closely integrated propulsors.

The power balance is formulated on a control volume \mathcal{V} with inner boundary \mathcal{S} covering the body surface and spanning the propulsor inlet and exit planes, and an outer boundary effectively at infinity. The boundaries have a unit normal \hat{n} defined out of the volume and hence into the body. The power balance equation for this volume is

$$F_X V_\infty = \Phi_\infty - P_K - P_V \quad (1)$$

where V_∞ is the freestream speed, and F_X is the net streamwise force on the body (including the propulsor inlet and exit) defined by

$$F_X V_\infty \equiv \oint \left[(p - p_\infty) \hat{n} - \bar{\tau} \cdot \hat{n} + \rho \mathbf{V} (\mathbf{V} \cdot \hat{n}) \right] \cdot \mathbf{V}_\infty d\mathcal{S} \quad (2)$$

The preceding is the usual streamwise force on the body defined in terms of a surface integral of pressure ($p - p_\infty$) and shear stresses $\bar{\tau}$, and also includes momentum fluxes over any propulsor inlet and outlet surfaces.

The net mechanical flow power passing through the propulsor inlet and exit is

$$P_K \equiv \oint \left[p_\infty - p + \frac{1}{2} \rho (V_\infty^2 - V^2) \right] \mathbf{V} \cdot \hat{n} d\mathcal{S} \quad (3)$$

which for an incompressible flow is equal to the total pressure flux. Incompressible:

$$P_K = \oint (p_{t_\infty} - p_t) \mathbf{V} \cdot \hat{n} d\mathcal{S} \quad (4)$$

The volumetric flow power

$$P_V \equiv \iiint (p - p_\infty) \nabla \cdot \mathbf{V} d\mathcal{V} \quad (5)$$

is a “ $p dv$ ” power, which is negligible for low-speed flows, and it is assumed that $P_V = 0$ in this study, an assumption that is assessed in Sec. V.D.2. The volumetric viscous dissipation is

$$\Phi_\infty \equiv \iiint (\bar{\tau} \cdot \nabla) \cdot \mathbf{V} d\mathcal{V} \quad (6)$$

$$= \Phi_{\text{jet}} + \Phi_{\text{surf}} + \Phi_{\text{wake}} + \Phi_{\text{vortex}} \quad (7)$$

and is the sum of all the dissipation sources in the flowfield, as illustrated in Fig. 4.

For a conventional non-BLI configuration, the combined dissipation $\Phi_{\text{surf}} + \Phi_{\text{wake}}$ is the usual profile drag power (profile drag force times freestream velocity), with the first term describing losses in the boundary layers and the second term losses in the wakes. The surface dissipation in the airframe's boundary layers Φ_{surf} is only

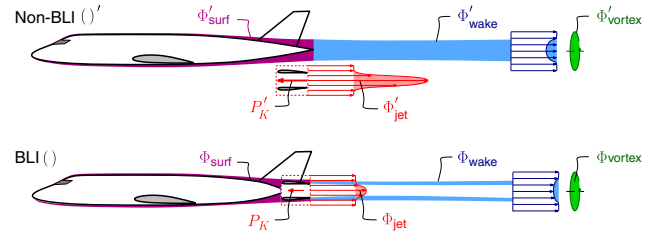


Fig. 4 Illustration of power balance terms for (bottom) boundary layer ingesting and (top) conventional aircraft.

weakly affected by BLI when ingestion occurs at the trailing edge [20], as is the case for the D8. The vortex dissipation Φ_{vortex} is the conventional induced drag power and is the same for non-BLI and BLI configurations that have the same lift and spanwise lift distribution, as discussed in Sec. V.A.

Within the power balance framework, the action of BLI can be understood as a reduction of the dissipation in the jet and wake (i.e., a reduction in the wasted kinetic energy left by the aircraft when the propulsors “reenergize” the wake), as sketched in the bottom of Figs. 1 and 4. The reduced $\Phi_{\text{jet}} + \Phi_{\text{wake}}$ translates directly via Eq. (1) to a reduction in the propulsor power P_K required to produce a force F_X .

As mentioned earlier, the benefit of BLI may be partially offset by the effect of the distorted propulsor inflow on fan performance. The fan-efficiency effect is thus separated from BLI's propulsive-efficiency effect by using P_K as the performance metric and a surrogate for fuel burn. More specifically, because P_K is defined only on the propulsor inlet and exit planes, it does not explicitly depend on fan characteristics, such as operating point, efficiency, and distortion response. Losses internal to the propulsor are thus immaterial to its effect on the external flowfield and net streamwise force.

The power balance framework is employed in this work for the comparison of non-BLI and BLI configurations, and the benefit of BLI is measured in terms of mechanical flow power.

B. Performance Parameters

1. BLI Benefit

The benefits of BLI can be separated into two parts. First, BLI provides an aerodynamic benefit, which is defined as consisting of the propulsive benefits of reducing jet and wake losses and of the external aerodynamic benefits resulting from reducing nacelle surface friction losses. Henceforth, these aerodynamic benefits of BLI are referred to as the aerodynamic BLI benefit for short. An additional, system-level benefit is enabled by BLI and is the result of reductions in engine and nacelle weights and the compounding effect of overall aircraft weight reduction: A lighter engine results in a lighter aircraft, which in turn requires less power and thus enables an even smaller and lighter engine.

The goal of the present study is to quantify the aerodynamic benefit of BLI, which is hereafter also simply referred to as the BLI benefit. In this sense, BLI reduces the propulsor flow power required to achieve a net streamwise force on the aircraft. Following Smith [15], the aerodynamic BLI benefit is quantified via the power saving coefficient (PSC), which in terms of mechanical flow power is

$$\text{PSC} \equiv \frac{P'_K - P_K}{P'_K} = 1 - \frac{P_K}{P'_K} \quad (8)$$

where a prime ($'$) indicates quantities for the non-BLI configuration, and the comparison is done at a set net streamwise force. The benefit is thus the difference in power required to produce a given net streamwise force.

The BLI benefit is a function of the aircraft operating parameters, namely, lift and streamwise force coefficients C_L and C_X . In the experiments, these parameters were varied by specifying the model angle of attack α and the motor power input (or wheel speed).

Two independent methods were used to calculate P_K : 1) the *direct method*, in which the flowfield measured using flow surveys is

integrated to obtain P_K from its definition (4); and 2) the *indirect method*, in which electrical power is recorded during the wind-tunnel tests and converted to flow power using offline measurements of the related efficiency.

2. Net Streamwise Force

Thrust and drag forces are ambiguous in a BLI system, so instead the net streamwise force F_X , or drag minus thrust, is used because it is always well defined. Its nondimensional form is the streamwise force coefficient

$$C_X \equiv \frac{F_X}{q_\infty S_{\text{ref}}} \quad (9)$$

with a negative value indicating a forward net aerodynamic force.

3. Net Propulsor Power: Direct Method

One method of determining P_K is via surveys of the propulsor in- and outflow planes. Measurements of the pressure fields, velocity magnitudes, and flow directions are used to calculate P_K from Eq. (4) using numerical integration. This method of obtaining P_K is referred to as the direct method. The nondimensionalized form is the flow power coefficient

$$C_{P_K} \equiv \frac{P_K}{q_\infty V_\infty S_{\text{ref}}} \quad (10)$$

4. Electrical Power: Indirect Method

A second way to calculate the propulsor power P_K is via the measured electrical power supplied to the motor P_E together with motor and fan efficiencies η_m and η_f , respectively, determined in separate offline experiments. The electrical power coefficient is defined as

$$C_{P_E} \equiv \frac{P_E}{q_\infty V_\infty S_{\text{ref}}} \quad (11)$$

and the two power coefficients are related through

$$C_{P_K} = \eta_f \eta_m C_{P_E} \quad (12)$$

which is the relation used in the indirect method to obtain P_K . In contrast to flow surveys, electrical motor power can be measured reliably and instantly during the wind-tunnel tests. Its disadvantage is that the offline motor and fan-efficiency measurements introduce additional uncertainties in the resulting C_{P_K} value.

Note that the C_{P_K} values given for this and the direct method are the sum of the contributions from the two (left and right) propulsors (i.e., the total power for the configuration is always reported).

III. Experimental Measurement of BLI Benefit

In this section, the major features of the experimental models, approach, and data postprocessing are summarized. Further details can be found in [21].

A. D8 Model Configurations

To ensure correspondence between experiments and full-scale aircraft, the model airframe and fan diameter are geometrically scaled. The propulsor operating points are selected to match the full-scale airframe lift and net streamwise force coefficients at cruise.

The aerodynamic BLI benefit for the D8 aircraft is measured by comparing the performance of two 1:11-scale powered wind-tunnel models (1:11 scale nominally; actual scale is 1:11.16): the non-BLI configuration has podded propulsors that ingest freestream flow and serve as baseline; the BLI configuration has propulsors embedded in the aft upper fuselage that ingest part of the fuselage boundary layer. A third, unpowered configuration is used to measure the aerodynamic characteristics of the airframe. To remove extraneous variability and

facilitate comparison, the three configurations share the majority of their components.

1. Common-Body Geometry

The three model configurations share the same physical components, except for the removable aft 20% of the fuselage and attached vertical tails (the horizontal tail is common). The front fuselage and wing geometry were defined during the Phase 1 Project [10,11]. Numerical simulations showed no reason for altering the design, and the front fuselage and wing were used unchanged for the 1:11-scale model experiments. The rear 20% of the fuselage and propulsion sections were designed as part of phase 2. Table 1 gives major model dimensions.

All the model surfaces (wings, fuselage, tails, and propulsor nacelles) are tripped to obtain turbulent flow. Adequacy of the trips was determined by verifying that a uniform increase in drag coefficient with decreasing tunnel speed was observed. This indicated absence of laminarization with decreasing Reynolds number and the presence of fully turbulent boundary layers at the conditions at which the BLI-benefit measurement is performed.

2. Unpowered Configuration

The unpowered configuration consists of the D8 common body and the tail from the non-BLI configuration, with no pylons or propulsors. The design aimed to keep the rear of the fuselage unloaded to preserve the configuration spanwise loading and to leave the pitching moment unaffected. The vertical tails were designed to be unloaded in zero-yaw flow conditions, which was accomplished by toeing out the lower (root) profile of the vertical tails by 3 deg and the upper (tip) profile by 1.5 deg to match the local flow angles.

3. Electric Propulsors

The non-BLI and BLI model configurations are powered by the same two propulsor units, each consisting of a fan stage (rotor and stator), electric motor, centerbody, aluminum housing, nozzle, and power electronics. The fan stages are carbon-composite TF8000 ducted fans manufactured by Aeronaut for use on remote control airplanes. At 5.65 in diameter, they are composed of a five-blade rotor and a four-blade stator. Each propulsor is driven by a 2 kW brushless dc electric motor. This paper presents results obtained with a nozzle to fan area ratio of $A_{\text{nozzle}}/A_{\text{fan}} = 0.604$.

The propulsors were designed so that the rotor, stator, internal ducting, centerbody, nozzle, and motor comprise a single removable unit that is separate from the outer nacelle and can be interchanged between the non-BLI and the BLI configurations. Each physical propulsor unit had a designated side (i.e., on the model left or right side) and was used exclusively on that side. Figure 5 shows the propulsors with the non-BLI and BLI support nacelle structures indicated in gray.

4. Non-BLI Configuration

The non-BLI configuration has the propulsor units embedded in axisymmetric nacelles, mounted on pylons at the rear of the aircraft, as shown in Fig. 6. The length of the pylon and angle at which it intersects the fuselage were chosen such that the surface pressure change on the nearby fuselage was less than $|\Delta C_p| < 0.03$, and so this installation represents an “isolated” propulsion system that serves as a control case for the BLI installation. The pylon airfoil cross section

Table 1 Reference dimensions of the 1:11-scale D8 models

Dimension	Value	
Reference area, S_{ref}	1.088 m ²	1686.0 in. ²
Reference chord, c	0.273 m	10.75 in.
Span	4.097 m	161.3 in.
Overall length of non-BLI configuration	3.218 m	126.7 in.
Overall length of BLI configuration	3.138 m	123.6 in.
Propulsor fan diameter, d_{fan}	0.144 m	5.65 in.
Propulsor fan area, excluding hub, A_{fan}	0.0159 m ²	24.6 in. ²

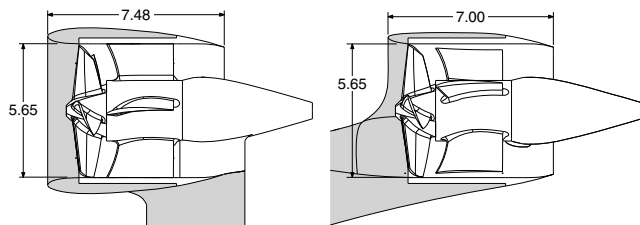


Fig. 5 Propulsors in (left) non-BLI and (right) BLI installations. Unshaded parts are common to both configurations, and the grayed regions show the nacelles and support structures specific to each configuration. Units are in inches.

was made as small as the installation and structural considerations allowed to make the non-BLI configuration as efficient as possible and avoid artificially inflating the BLI benefits. (This was confirmed from force measurements of the unpowered configuration with pylons attached and smooth rounded caps at the free ends instead of propulsors. These forces were found to be indistinguishable from forces recorded on the unpowered model without pylons, indicating that the installed pylons drag was smaller than the force balance measurement precision.) The propulsor axis is toed out by 2 deg relative to the model's longitudinal direction to align the propulsor with the local flow.

5. BLI Configuration

The BLI configuration has propulsor units embedded in the rear fuselage, as shown in Figs. 7 and 8. The whole fuselage rear (upper and lower surfaces), vertical tails, and propulsor nacelles were designed as an aerodynamically integrated geometry to provide the desired diffusion upstream of the fan, while avoiding aerodynamic interference between the upper-half nacelles and the tail surfaces. It must be emphasized that the aerodynamic design is considered as "good enough," in that the design objective was elimination of any obvious problems such as unnecessary local

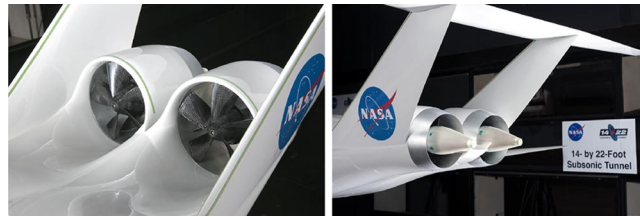


Fig. 8 Close view of the BLI configuration model tail in NASA Langley 14- by 22-foot subsonic tunnel during the August–September 2013 experiments (photo credits: NASA/George Homich).

overspeeds and flow separations, and is not "optimal" in a rigorous sense. It is likely that it could be improved with more extensive design work.

The vertical tails have a 7 deg toe-out angle at their roots to align them with the flow contraction produced by the presence of the integrated propulsors. The half-nacelles over the BLI propulsors were designed with a smaller thickness and leading-edge overhang than the non-BLI podded nacelles, as can be seen in Fig. 5. The design objectives for the half-nacelles were to limit the overspeed inside the nacelle lip at high engine power and to obtain a positive pressure coefficient with weak streamwise pressure gradients over the outside nacelle surfaces. These features reduce skin friction losses and eliminate the need for fillets in the tight inside corners between the two nacelles and between each nacelle and the adjoining vertical tail.

The propulsor axis is offset relative to the model axes to align the propulsor with the local flow: It is pitched up by 3 deg and toed-out by 1.5 deg relative to the model's longitudinal direction.

B. Experimental Approach

1. Wind Tunnel

Measurements were conducted in the 14- by 22-foot subsonic tunnel at the NASA Langley Research Center, with a closed rectangular cross section of 14.5×21.75 ft (4.42×6.63 m). The

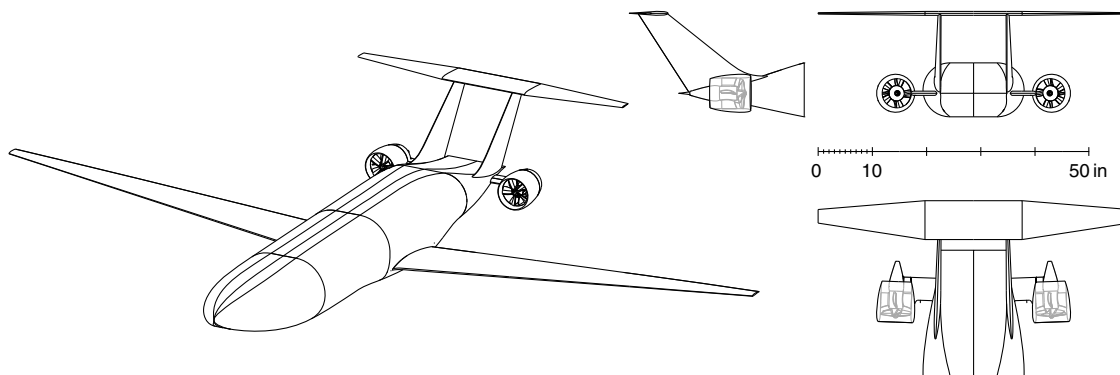


Fig. 6 Non-BLI model configuration.

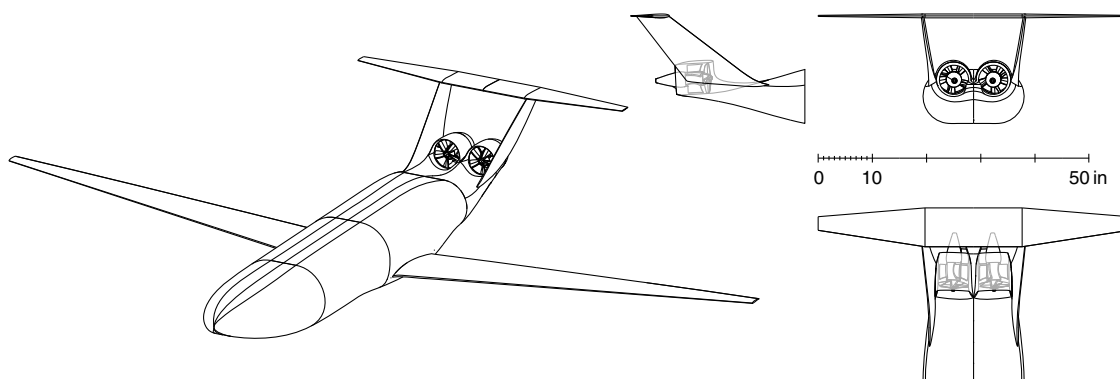


Fig. 7 BLI model configuration.

model is attached near the wing root's quarter-chord to a pitch-head and trunnion mounting system, which control angle of attack and height.

The model is vertically positioned so that a reference point near the wing root leading edge is held at the center of the tunnel test section as the angle of attack is changed. At zero angle of attack, the wind-tunnel blockage (ratio of model to test section cross-sectional areas) is approximately 0.5%.

2. Test Procedures

The majority of the experiments were performed at tunnel speeds of 70 and 84 mph (31.3 and 37.5 m/s), corresponding to Reynolds numbers based on model reference chord of 0.57×10^6 and 0.68×10^6 , respectively, and Mach numbers of 0.092 and 0.110. The reference quantities for these speeds are listed in Table 2, and the propulsor nondimensional fan wheel speeds are given in Table 3.

The common body of the D8 was mounted on the pitch head and trunnion via an internal force balance at the beginning of each test campaign and not removed until the conclusion of the tests, with changes between configurations undertaken in situ. The model center of gravity is located approximately 5 in. (0.13 m) aft of the force balance reference center. After any configuration change, load checks were performed to verify the model instrumentation and to rule out any fouling between metric and nonmetric components. Weight tares, or wind-off force readings, were obtained before and after every set of runs.

3. Run Types

Three main types of runs were performed:

1) Angle-of-attack sweeps were performed for the unpowered configuration. At a fixed tunnel velocity V_∞ , the model angle of attack α was varied (typically from 0 to 8 deg), and the forces on the model were recorded.

2) Power sweeps were performed for the powered configurations, with and without BLI. At a fixed tunnel velocity V_∞ and fixed model angle of attack α , the power input to the propulsor was varied by changing the wheel speed Ω , and the forces were recorded at each power level.

3) Flow surveys were performed for the powered configurations with the survey system attached to the model support and indexed on the model, and the flow measuring probe was set to survey either the inlet or exit of one of the propulsors. Each survey was performed at a fixed tunnel velocity V_∞ , fixed model angle of attack α , and fixed wheel speed Ω .

Additional measurements were taken at conditions that simulate takeoff, top of climb, and descent, as well as cases with yaw angles up to ± 30 deg and with one propulsor out. The results of these off-cruise measurements will be discussed in a future publication: They revealed no problem areas for the propulsors in spite of high-distortion levels.

Table 2 Tunnel nominal operating conditions

Freestream velocity V_∞		Dynamic pressure q_∞		M_∞	Re_c
mph	m/s	Pa	psf		
70	31.3	598	12.5	0.092	0.57×10^6
80	37.5	861	18.0	0.110	0.68×10^6

Table 3 Propulsor dimensional and nondimensional wheel speeds, Ω and U_{tip}/V_∞ , used in power sweeps

Ω , rpm		8000	10,600	12,250	13,500	14,500
U_{tip}/V_∞ at	$V_\infty = 70$ mph	1.93	2.55	2.95	3.25	3.49
	$V_\infty = 84$ mph	1.61	2.13	2.46	2.71	2.91

4. Force Measurements

The forces and moments on the model were measured using the NASA 843A six-component internal force balance, calibrated at NASA Langley specifically for these tests. They are measured in the model axes system and rotated to the freestream axes using the angle of attack measured by a NASA Q-flex accelerometer mounted on the model near the balance location.

No wind-tunnel corrections are applied and forces are reported as uncorrected values. The main reason for this choice is that the focus of this work is on the relative changes between non-BLI and BLI configurations, which would have the same (small) wind-tunnel corrections because they have the same blockage and the same C_L . Therefore, the BLI benefit would not be affected by any such corrections.^{†††}

The forces have the model weight contributions removed using wind-off weight tare measurements, so that F_X and F_Z (and the corresponding coefficients C_X and C_L) are the aerodynamic forces on the entire model, including its propulsors.^{†††} The models have fixed solid horizontal tails with no provision to adjust or trim the pitching moment during the experiments, and no correction is made to the data to bring it to a zero pitching moment condition. This is justified by the fact that such trimming has a negligible effect on the net streamwise force and the BLI benefit at cruise, as shown in Sec. V.B and [21].

5. Electrical Power Measurements

The electrical power drawn by the propulsors is calculated as the product of the continuous reading of voltage and current out of the power supply. The fan wheel speed is determined from the motor controller voltage frequency.

6. Flow Surveys

For the 2013 tunnel tests, rotating rakes of total and static pressure tubes were used to survey the flow upstream propulsor inlet and downstream of the nacelle exit plane. Detailed descriptions of the rake system and data processing are given in [26,27].

During the 2014 tests, five-hole probes (FHP) were used to obtain flow angularity information at the propulsor inlet and exit planes in addition to pressure data. The survey planes were located closer to the propulsor than what was possible with the pressure rakes. Details of the five-hole-probe surveying system and ingested flow measurements will be the subject of a future publication.

C. Postprocessing of Experimental Data

1. Simulated Cruise

The simulated cruise condition is defined as $C_L = 0.64$ and $C_X = 0$. This lift coefficient value, which occurs at approximately 2 deg angle of attack, is that of the full-size D8 aircraft. The net streamwise force is varied by changing the propulsor motor power via fan wheel speed, with the exact $C_X = 0$ point obtained by interpolation between measurements using a curve fit of the C_X versus C_{P_K} data.

2. Correction to a Specified C_L

To evaluate the aerodynamic benefit of BLI at cruise condition, it is appropriate to compare the power required by BLI and non-BLI configurations at the same lift coefficient as the full-size D8 aircraft, $C_L = 0.64$.

During the tests, the model angle of attack was found to change when the propulsor power was varied, through compliance of the force balance, due to lift-producing changes in the flow around the

^{†††}It should also be noted that the wind-tunnel corrections were computed using the NASA Langley 14- by 22-foot subsonic-tunnel facility procedures for classical wall corrections and were found to be of the same order as the uncertainty in force measurements at the cruise condition.

^{†††}The weight of the model mounted in the wind tunnel as measured by the force balance is recorded without freestream flow. This so-called wind-off weight is then subtracted (used as a tare) from the force measured with the tunnel running to obtain the aerodynamic force on the model defined as the total force minus the weight.

nacelles and reduced pressure on the top aft fuselage of the BLI configuration.

Adjusting the model support system angle for each power setting to maintain exactly the desired C_L value was deemed impractical due to the large number of runs and data points taken. Instead, the angle of attack (and hence C_L) is set at the beginning of each run, and the measured streamwise force coefficient is corrected offline, as detailed in Appendix A. The correction is small enough not to add any significant uncertainty to the reported results.

3. Direct Method: Mechanical Flow Power from Flowfield

To find the mechanical flow power via the direct method, the measurements taken during the flow surveys are used with the exit streamtube integration area determined based on a threshold minimum total pressure. When the rakes are used, the inlet integration area at the upstream rake survey plane is determined from computational fluid dynamics computations of the D8. Details on how the integration is carried out, as well as sensitivities and uncertainty analyses, can be found in [26,27]. When the FHP is used, given the close proximity of the probe to the nacelle leading edge, the inlet integration is performed on a circular area with a diameter equal to that of the fan.

4. Indirect Method: Power Conversion from Electrical to Mechanical

In the indirect method, the conversion between electrical and mechanical power is made using the fan pressure-rise and efficiency characteristics measured at MIT in a 1×1 ft wind tunnel with uniform upstream flow and with a distortion representative of the ingested fuselage boundary layer as discussed in [28,29]. Data were taken at conditions that span the full range of electrical power levels. At each condition, a five-hole-probe survey was performed at the propulsor inlet and exit planes to determine the mass flow (or flow coefficient ϕ) and mechanical flow power P_K . These calibration experiments allow the conversion from electrical power to mechanical flow power via the relation $P_K = \eta_o P_E$. The motor efficiency η_m , known from motor characterization experiments as a function of wheel speed [30], is used to compute the fan efficiency $\eta_f = \eta_o / \eta_m$.

5. Curve Fits and Confidence Interval

During the Langley experiments, data were taken for at least 10 repeat runs at any given condition. Each cluster of points in a C_X versus C_{P_K} plot represents a set of repeat runs, and the scatter of the cluster is a measure of the experimental repeatability.

Curve fits for C_X versus C_{P_K} for each configuration are constructed based on second-order polynomials as detailed in Appendix A. The value of the power at cruise is taken from the C_{P_K} (C_X) fitted curve at $C_X = 0$, and the reported experimentally measured BLI benefit, or power-saving coefficient, is thus based on the curve fits. Regression statistical analysis [31] is performed to obtain the 95% confidence interval for each configuration, yielding in turn the confidence interval on the benefit at cruise as explained in Appendix A.

IV. Aerodynamic BLI Benefit Results

A. Benefit at Equal Nozzle Area: Force Versus Power

Figure 9 compares the measured net streamwise force coefficient C_X of the BLI and non-BLI configurations over a range of power levels C_{P_K} at the simulated cruise value of $C_L = 0.64$. The figure shows as symbols the data taken during the two wind-tunnel test campaigns at both Reynolds numbers of 0.57×10^6 and 0.68×10^6 and processed using the indirect method and the direct method with both pressure rakes and FHP. The results for the unpowered configuration, for which the net streamwise force is indicative of the drag of the non-BLI configuration airframe, are shown at $C_{P_K} = 0$.

The lines in the upper plot in Fig. 9 correspond to the polynomial data fits obtained with the indirect method. The bottom plot gives a zoomed-in view of the same data near the simulated cruise condition of $C_X = 0$, with dashed lines indicating the 95% confidence interval for each configuration.

The distance between the BLI and non-BLI curves provides an experimental measure of the BLI benefit and demonstrates an aerodynamic benefit from BLI. The BLI configuration consistently requires less power to produce the same streamwise force than the non-BLI configuration, and this power reduction is observed through the full range of power settings, from idle to max wheel speed.

There are no statistically significant differences between data points taken at the two different Reynolds numbers; the spread between points at the same Re_c is comparable to the differences between Reynolds numbers, indicating Reynolds numbers effects are negligible and that these low-speed results can be scaled to flight Reynolds numbers. Furthermore, the repeatability between test campaigns is excellent, because it is not possible to discern between indirect method measurements taken during the first test campaign and those of the second campaign.

The good agreement between the power values using the two methods (direct and indirect) gives confidence in the results. The largest discrepancy in C_{P_K} between the two methods is approximately 5% and is observed for the BLI configuration. The difference can be attributed to uncertainty in the shape and extent of the captured streamtube, which leads to error in the contribution of C_{P_K} at the inlet measurement plane for the direct method, a contribution which represents approximately 10% of total C_{P_K} .

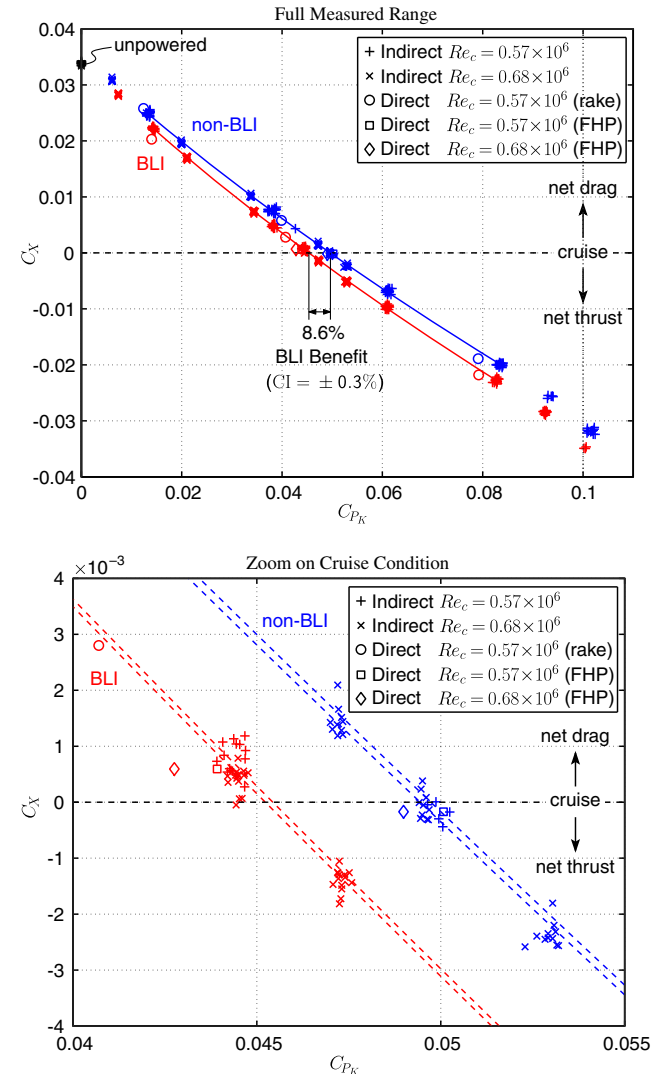


Fig. 9 Net streamwise force coefficient versus mechanical flow power coefficient at $C_L = 0.64$: (top) full measured range and (bottom) zoom on cruise condition. For each of the configurations, symbols are experimental measurements, solid lines on the top plot show curve fits to data points obtained using the indirect method, and dashed lines on the bottom plot show the 95% confidence interval.

Figure 9 summarizes a major finding, namely, the difference in power required between the BLI and the non-BLI configurations, represented by the horizontal offset between the corresponding curves. This is the power-reduction benefit of BLI at equal nozzle area and exists over a wide range of C_{P_K} settings and corresponding C_X values, from descent to climb. At the cruise condition of $C_X = 0$, this aerodynamic BLI benefit is $PSC = 8.6\%$. Other quantities of interest are given in Table 4.

Based on the uncertainty analysis detailed in Appendix B, the experimentally measured aerodynamic BLI benefit is quoted as $PSC = (8.6 \pm 1.8)\%$. The corresponding fractional uncertainty is $\pm 1.8/8.6\% = \pm 0.21$, and the confidence interval fraction, which is a measure of repeatability, is $CI_{PSC} = \pm 0.3/8.6\% = \pm 0.035$. These results give confidence that a significant fuel burn reduction could be realized for a full-size aircraft.

B. Left-Right Power Asymmetry

The two propulsors in the non-BLI configuration have symmetrical operating characteristics in that they require the same power for any fan wheel speed. When installed on the BLI configuration, however, the right propulsor unit requires more power than the left one to maintain the same wheel speed, and the asymmetry increases with angle of attack. The right propulsor required about 6% more power than the left propulsor at $\alpha = 2^\circ$ and 19% more power at 6 deg [12]. To put this asymmetry in context, if it were created by inlet guide vanes that turned the flow uniformly, the swirl angle would be roughly 3 deg.

In wind-off static operation, the power was found to be symmetric for both configurations, thus ruling out hardware differences being the cause. The power asymmetry is therefore hypothesized to be due to crossflow in the ingested fuselage boundary layer. The crossflow, observed in tuft flow visualizations such as in Fig. 10, is outboard from the fuselage centerline, as sketched in the top left of Fig. 11. The crossflow angles are symmetric with respect to reflection about the aircraft centerline, but the two fans have the same right-hand rotation, giving an asymmetric interaction between the crossflow and the fan blades, as sketched in the middle left of Fig. 11. The crossflow velocity is coflowing for the left fan blades (moving in the same direction as the rotor), and counterflowing for the right fan blades (moving opposite to the rotor).

The bottom left of Fig. 11 shows velocity triangles seen by the left and right blades at the bottom 180 deg position, for the two fans at the same wheel speed, the way in which the experiments were carried out. The right fan blades see a larger incidence angle and a larger relative velocity, and hence are more highly loaded than the left fan blades. The larger crossflow and swirl velocity observed with increasing angle of attack increases the asymmetry in the blade loading consistent with the larger measured power asymmetry at higher angle.

The blade aerodynamic loading versus azimuthal angle is sketched on the top right of Fig. 11. Averaged over the blade path, the right fan has a greater torque, and requires more power, than the left fan. This left/right power asymmetry is not necessarily detrimental, because the right propulsor draws more power but also adds more power to the flow than the left propulsor, through a basically inviscid shift in fan operating point. The total (left plus right) power is not influenced by the asymmetry, as long as the operating points for both propulsors remain near peak efficiency and away from stall.

Table 4 Summary of experimental results at simulated cruise

Case	Values				
Configuration quantities	C_{P_E}	$C_{P_{Shaft}}$	C_{P_K}	P_K/P'_K	PSC
Non-BLI	0.0707	0.0568	0.0496	1	0
BLI	0.0655	0.0526	0.0453	0.913	8.6%
Propulsor quantities	V_{jet}/V_∞	U_{tip}/V_∞	ϕ	η_f	η_p
Non-BLI	1.66	2.79	0.361	0.878	0.752
BLI	1.60	2.71	0.354	0.863	0.775

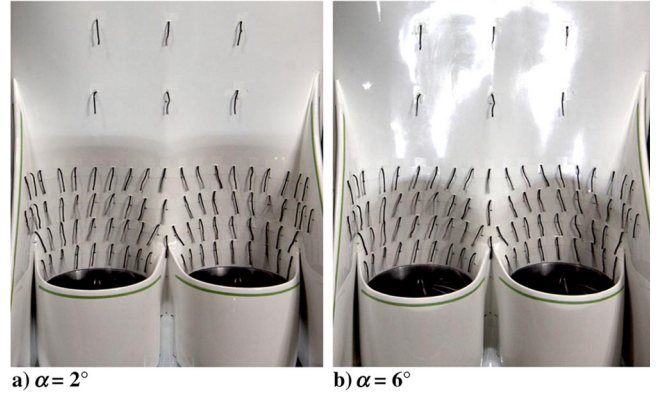


Fig. 10 Tufts on fuselage upstream of propulsor inlets at $Re_c = 0.57 \times 10^6$, $U_{tip}/V_\infty = 2.95$, showing outward crossflow in the fuselage boundary layer entering the propulsor fans. The crossflow is larger in the $\alpha = 6^\circ$ case (right).

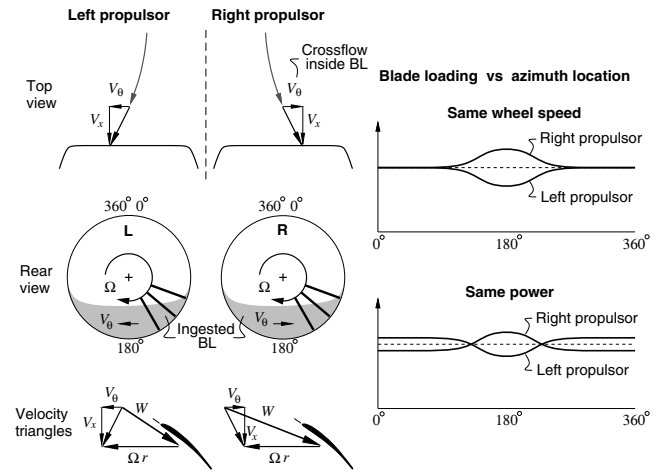


Fig. 11 Illustration of crossflow-induced blade loading differences between left and right propulsors in BLI configuration.

V. Applicability of Experimental Results

A. Vortex Dissipation (Induced Drag) Effects

The design wingspan and spanwise loading distribution of a transport aircraft are typically determined by a tradeoff between structural weight and vortex dissipation (or the equivalent induced drag). This tradeoff is not influenced by the presence or absence of BLI, and therefore an objective in the experiments was to make the BLI and non-BLI configurations have the same vortex dissipation so that the BLI benefit measured is associated with propulsion aerodynamics alone.

Both configurations have the same wings, horizontal tail, and most of the fuselage, and thus are expected to have nearly the same lift characteristics and spanwise load distributions. However, the propulsor power level influences the pressure field upstream of the propulsor and therefore affects the lift distribution on the rear BLI-configuration fuselage. The results between configurations are compared at the same lift coefficient, but there is a possibility that the span efficiency be changed and that some of the measured BLI benefit be due to changes in vortex dissipation. This effect is examined here and shown to be negligible.

An expression for the streamwise force coefficient is obtained from the nondimensional form of the power balance (1) with the breakup of dissipation contributions:

$$C_X = C_{\Phi_{wing}} + C_{\Phi_{other}} + C_{\Phi_{vortex}} - (C_{P_K} - C_{\Phi_{jet}}) \quad (13)$$

Here, $C_{\Phi_{wing}}$ is the coefficient of dissipation in the wing boundary layer and viscous wake, whereas $C_{\Phi_{other}}$ is the dissipation in the boundary layers and wakes of the remaining airframe components:

fuselage, tails, and nacelles. Given the D8's geometry, it is reasonable to assume that the wing viscous flow and the overall trailing vortex system do not interact with the propulsors and therefore to write

$$C_{\Phi_{\text{wing}}} = C_{D_{\text{wing}}}(C_L) \quad (14)$$

and

$$C_{\Phi_{\text{vortex}}} = C_{D_i}(C_L) = \frac{C_L^2}{\pi Re} \quad (15)$$

where $C_{D_{\text{wing}}}$ is the wing's conventional profile drag coefficient and C_{D_i} is the conventional induced drag coefficient. Relation (15) implicitly defines the span efficiency e , which is a function only of the shape of the spanwise load distribution.^{§§§}

Using relations (14) and (15), the power balance Eq. (13) becomes

$$C_X - C_{D_{\text{wing}}} = \frac{C_L^2}{\pi Re} + [C_{\Phi_{\text{other}}} - (C_{P_K} - C_{\Phi_{\text{jet}}})] \quad (16)$$

in which terms in the brackets are expected to be nearly independent of C_L . The term $C_{\Phi_{\text{other}}}$ consists of the viscous dissipation of the fuselage and the nearly nonlifting tail, whose tripped turbulent boundary layers see only weak adverse pressure gradients over the modest range of angles of attack between 2 and 8 deg considered here, and so their dissipation will not change appreciably. Furthermore, with the propulsor wheel speed held fixed, the propulsor flow also will not change, and the combination $(C_{P_K} - C_{\Phi_{\text{jet}}})$ will be independent of C_L .

For a moderately high aspect ratio low-sweep wing, such as the one on the D8 model, the $C_{D_{\text{wing}}}$ versus C_L relation can be approximated as the chord-weighted average of the two-dimensional airfoil drag coefficients across the span. These can be obtained from two-dimensional viscous airfoil calculations using XFOIL [32] for the five airfoil sections that define the wing geometry, with tripped boundary layers to reflect the trips on the model. The wing's overall profile drag polar implied by these section polars is approximated by the curve-fit function

$$C_{D_{\text{wing}}}(C_L) \approx 0.0114 + 0.0005C_L + 0.0022C_L^2 + 0.0002C_L^{12} \quad (17)$$

A series of wind-tunnel operating points for all three configurations is now examined for varying angle of attack and at $Re_c = 0.57 \times 10^6$. For each point, the value of $C_{D_{\text{wing}}}$ is estimated from the curve fit (17) using the measured C_L . The resulting plots of $C_X - C_{D_{\text{wing}}}$ versus C_L^2 are shown in Fig. 12, together with lines of slope $1/(\pi AR)$ representing the ideal fan efficiency $e = 1$ along the points for each configuration. For the powered configurations, the propulsor wheel speed is held fixed at $U_{\text{tip}}/V_\infty = 2.55$. With the previously discussed assumption that the three terms in the brackets in Eq. (16) are independent of C_L , any variation in the data points in Fig. 12 for any one configuration must be entirely due to the remaining C_L^2 term, for which

$$\frac{\partial(C_X - C_{D_{\text{wing}}})}{\partial(C_L^2)} = \frac{1}{\pi Re} \quad (18)$$

Thus, any deviation of the data points from the straight lines in Fig. 12 can be attributed to a nonunity span efficiency.

The close fit of the data to the straight lines indicates that all three configurations have nearly $e = 1$, which seems surprisingly high.

^{§§§}The traditional Oswald span efficiency e_o is defined from the slope of the C_D versus C_L^2 curve, where $C_D \approx C_{D0} + C_L^2/(\pi Re_o)$, but the parasite drag C_{D0} does not represent all the surface and wake dissipation of the airframe. Instead, any profile drag creep with increasing C_L would be lumped into the C_L^2 term, where it would artificially modify the span efficiency value. The Oswald span efficiency is thus not a true measure of vortex dissipation.

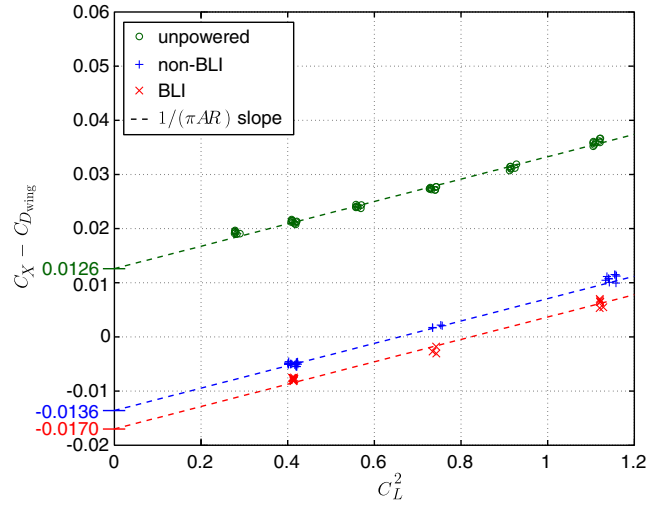


Fig. 12 Polar plots of $C_X - C_{D_{\text{wing}}}$ versus C_L^2 as measured experimentally at $Re_c = 0.57 \times 10^6$ (symbols), compared against lines with ideal ($e = 1$) induced drag slope $1/(\pi AR)$. Data for the BLI and non-BLI configurations are for fixed wheel speed of $U_{\text{tip}}/V_\infty = 2.55$. The close fit between symbols and lines imply the same span efficiency of $e \approx 1$ for all three configurations.

However, it should be noted that the assumed $C_{D_{\text{wing}}}(C_L)$ function (17) is only an estimate, and also that C_X is uncorrected for tunnel wall effects, which partially act as “ground effect” and tend to increase e . Regardless, the main conclusion from Fig. 12 is that all three configurations exhibit nearly the same span efficiency over the operating range of α between 2 and 8 deg. Therefore, variation in vortex dissipation (or induced drag) is not a factor in the measured BLI benefit, which is attributable only to propulsion aerodynamic effects as intended.

B. Trim Drag Effects

1. Pitch Trim

Steady cruise of an actual aircraft requires pitch trim (i.e., a zero pitching moment about the aircraft's center of gravity). Because the wind-tunnel models had fixed solid horizontal tails, there was no provision to achieve pitch trim during the tests, and therefore any associated trim drag that would be incurred by the actual aircraft is not represented in the C_X data. This missing trim drag is examined here and is shown to not significantly influence the BLI benefit.

The pitching moment coefficient values about the model's reference point C_m were measured during the tests and translated to new moment values about the center of gravity location $C_{m_{c.g.}}$, which would be needed to obtain a specified static margin as predicted by the AVL vortex lattice code.^{†††} The vortex lattice code was also used to calculate the elevator deflection that would be needed to obtain pitch trim, along with the slight adjustment to α needed to restore $C_L = 0.64$. The difference in computed induced drag ΔC_{D_i} between the trimmed and untrimmed cases provides an estimate of the trim drag $\Delta C_{X_{\text{trim}}}$. The corresponding propulsive power change needed to restore $C_X = 0$ is then the flight power penalty due to the trim drag

$$\Delta C_{P_{K_{\text{trim}}}} = -\frac{\partial C_{P_K}}{\partial C_X} \Delta C_{X_{\text{trim}}} \approx 1.5 \Delta C_{X_{\text{trim}}} \quad (19)$$

where the slope value $\partial C_{P_K}/\partial C_X \approx -1.5$ is obtained from the $C_{P_K}(C_X)$ data shown in Fig. 9.

These calculations were performed for both the non-BLI and BLI configurations to obtain the corresponding $\Delta C_{P_{K_{\text{trim}}}}$ and $\Delta C_{P_{K_{\text{trim}}}}$ values. The change in BLI benefit that would result from meeting the pitch trim requirement is then

^{†††}Data available online at <http://web.mit.edu/drela/Public/web/avl> [retrieved 2 May 2017].

$$\Delta PSC_{trim} = \frac{\Delta C'_{P_{Ktrim}} - \Delta C_{P_{Ktrim}}}{C'_{P_K}} \quad (20)$$

The results are summarized in Table 5. Interestingly, the BLI benefit actually increases slightly from the trim drag effects for small static margins (SM) and decreases slightly for larger static margins. Regardless, all the changes are considerably smaller than the measured BLI benefit uncertainty. Therefore, the trim drag effects do not significantly affect the BLI benefit results.

2. Yaw Trim

In addition to pitch trim, steady cruise requires yaw trim (i.e., a zero yawing moment about the aircraft's center of gravity). As discussed in Sec. IV.B, the right propulsor on the BLI configuration draws more power than the left one and will produce more forward force, an asymmetry that will induce a yaw moment on the BLI configuration. The effect that trimming the model in yaw would have on the BLI benefit can be estimated in the same way pitch trim was calculated.

At the cruise condition, the difference in yaw moment between the BLI and the non-BLI configurations is $\Delta C_n = 1.9 \times 10^{-4}$. AVL predicts that correcting for this difference via rudder deflection would change the induced drag and hence streamwise force by $\Delta C_{X_{trim}} = 4.3 \times 10^{-7}$, a negligible change that would not noticeably alter the BLI benefit.

C. Sensitivity to Analysis and Modeling Assumptions

Presented here is a summary of the sensitivity of the BLI benefit as computed via the indirect method to the various uncertainties and assumptions in the analysis (see [21] for full details). The benefit is found to be insensitive to the specific approximations used to compute flow power.

1. Reynolds Number Effects

To enable scaling of the test data up to full-scale Reynolds numbers, it is necessary to ensure that the trips are working as expected so that turbulent flow is present on all model surfaces. However, early testing of the unpowered configuration with the initial trips showed first an increase and then a decrease in the drag coefficient as the Reynolds number was increased, indicating the presence of significant amounts of laminar flow at the lowest speeds. Therefore, the thickness of the airframe trips was increased until the presence of mostly turbulent flow was indicated by the drag coefficient monotonically decreasing with Reynolds number. This process was done for the wing and fuselage trips separately. Transition to turbulent flow at the trips was also confirmed by infrared cameras.

The insensitivity of the airframe and propulsor characteristics to Reynolds number is evident in the $C_X(C_{P_K})$ and $C_X(U_{tip}/V_\infty)$ curves shown for the BLI configuration in Fig. 13, and the same behavior was observed for the non-BLI configuration. The data points all nearly collapse onto common curves, especially at the two highest Reynolds numbers of 0.57×10^6 and 0.68×10^6 used in the BLI benefit quantification.

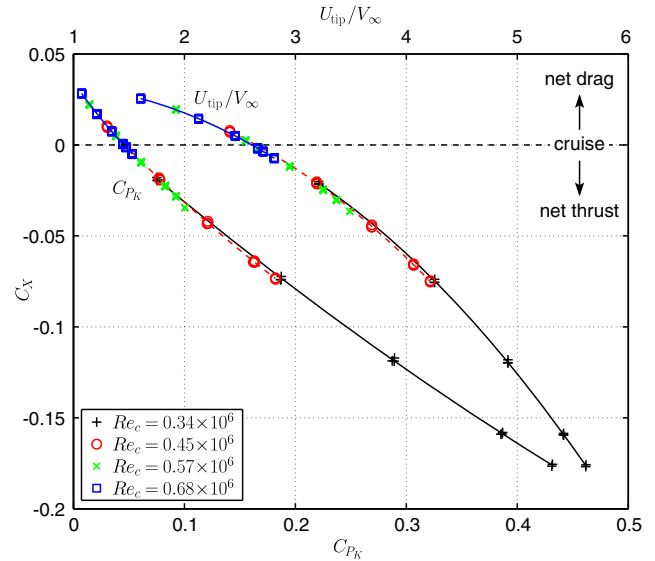


Fig. 13 Net streamwise force coefficient (bottom axis) versus mechanical flow power coefficient and (top axis) versus wheel speed at $C_L = 0.64$ for the BLI configuration at different Reynolds numbers.

2. Repeatability Between Test Campaigns

The data taken at $Re_c = 0.57 \times 10^6$ during the two test campaigns performed in the 14- by 22-foot subsonic tunnel in the summers of 2013 and of 2014 are now examined. Figure A1 in Appendix A shows lift and streamwise force coefficient measurements from both campaigns. The average difference in C_L between campaigns is 1.4% at the cruise lift coefficient of $C_L = 0.64$, with a difference in C_X of less than 0.2%. These differences are within the instrument precision of the force balance, and the repeatability between test campaigns is within the repeatability of a single campaign.

3. Effect of Correction to a Specified C_L

The measured BLI benefit of 8.6% at simulated cruise is found using a correction to match the desired $C_L = 0.64$ at all power levels. When a correction to a specified $\alpha = 2^\circ$ deg is employed instead, the benefit is 8.5%. With no corrections to either C_L or α , the benefit is found to be 8.7%. All these values are within the confidence interval of $\pm 0.3\%$, and so any errors linked to the correction to a specified C_L have a negligible effect on the BLI benefit.

D. Applicability to Full-Size Aircraft

1. Nondimensional Parameters

The applicability of the present aerodynamic model experiment to full scale requires matching all the relevant nondimensional parameters for the system being investigated, namely, the D8 aircraft with and without BLI propulsion. The relevant aerodynamic parameters that characterize the airframe are the geometry, lift coefficient C_L , Mach number M_∞ , and Reynolds number Re_c . Both the geometry and the lift coefficient of the scaled tests correspond to the full-size D8 aircraft.

Table 5 Differences in pitch trim corrections to C_X and C_{P_K} between BLI and non-BLI cases, and resulting change in BLI benefit due to trim ΔPSC_{trim} , for various static margins (SM)

SM	$\Delta C'_{X_{trim}} - \Delta C_{X_{trim}}$	$\Delta C'_{P_{Ktrim}} - \Delta C_{P_{Ktrim}}$	$\Delta PSC_{trim}, \%$
0.00	-0.387×10^{-4}	-0.580×10^{-4}	+0.13
0.05	-0.241×10^{-4}	-0.362×10^{-4}	+0.08
0.10	-0.094×10^{-4}	-0.141×10^{-4}	+0.03
0.15	0.051×10^{-4}	0.077×10^{-4}	+0.02
0.20	0.197×10^{-4}	0.296×10^{-4}	+0.07
0.25	0.341×10^{-4}	0.512×10^{-4}	+0.11

The Reynolds and Mach numbers are not matched, but these are not explicitly relevant to the BLI propulsion analysis in the power balance framework presented in Sec. II.A and as discussed further in [20]. Specifically, the BLI benefit is mostly due to 1) reduction in external losses resulting from the smaller nacelle wetted area and 2) propulsive-efficiency improvements that depend on the jet to freestream velocity ratio and the fraction of ingested to total kinetic energy defect (ingestion fraction). None of these controlling factors depend explicitly on Reynolds or Mach number, and they are matched between model and full-size aircraft.

The Reynolds number mismatch effect on the airframe is mitigated by applying boundary layer trips on all the surfaces, and so the resulting mostly turbulent profile drag could in principle be corrected to full-scale Reynolds numbers. No such correction is performed here because the focus is on the comparison of BLI and non-BLI configurations tested at the same Reynolds number. Although at full scale the total ingested kinetic energy defect would be smaller than in the experiments, the ingested fraction, and hence the BLI benefit, should be comparable.

The relevant parameters for the propulsion system are the nozzle to reference area ratio, the propulsor jet to freestream velocity ratio, and the ingested kinetic energy defect that is a fraction of airframe's surface dissipation [20]. These determine the propulsive power and the net streamwise force, and their values in the present experiments correspond to those for the full-scale D8 aircraft. Also matched is the propulsor streamtube contraction from freestream to fan face (ratio of captured streamtube areas between freestream and fan face), which could be sensitive to Mach and Reynolds numbers, and which is also equal to the velocity ratio $V_{\text{fan}}/V_{\infty}$, and to the factor of jet-to-freestream-velocity ratio and nozzle-to-fan-area ratio, all of which are the same for model and full-size D8.

The relevant aerodynamic parameters for the propulsor fan blading are fan Mach and Reynolds number. Although a fan designed for low Reynolds number operation was used, its pressure-rise characteristics are qualitatively similar to those of a transonic fan. For example, the observed drop of two percentage points in efficiency with distortion is in the range of what a jet engine fan is estimated to lose [18]. In terms of propulsive efficiency, the present experiments fall within the range of efficiencies predicted for the full-scale D8.

In summary, it is reasonable to conclude that the aerodynamic BLI benefit measured in the present low-speed tests is applicable to full-scale aircraft.

2. Compressibility Effects

In the power balance framework employed here, compressibility effects appear via the P_V term, via the density factor in the P_K definition, and via indirect effects of viscosity and density on the viscous and Reynolds stresses that impact the dissipation Φ_{∞} . Much of the present analysis, performance metrics, and BLI benefit estimation neglected these effects, specifically by dropping the P_V term from the power balance (1), and assuming constant density in all terms. These assumptions and approximations are much less restrictive than they might appear, due to various cancellations that occur in the formulation.

Integration of the Gibbs equation over any isentropic streamtube that starts and ends at freestream speed and pressure gives $P_V = 0$ for that streamtube. Therefore, all such isentropic streamtubes have zero net contribution to the overall P_V integral for the entire control volume. Integration of the Gibbs equation for an isentropic streamtube ingested by the propulsor (e.g., as in the non-BLI case) gives $P_{K_{\text{inlet}}} + P_{V_{\text{inlet}}} = 0$. Thus, making the two incompressible assumptions of neglecting $P_{V_{\text{inlet}}}$ and setting $P_{K_{\text{inlet}}} = 0$, via the Bernoulli equation used to obtain the incompressible P_K expression (4), gives a combined result that is exact even for the compressible case.

The neglect of the P_V contribution at the propulsor exit streamtube is based on assuming $p = p_{\infty}$ for the entire propulsor jet, which is a reasonable approximation even for compressible flows. A significantly under- or overexpanded supersonic jet generally does not appear on transport aircraft, especially not at cruise condition and with modern low fan pressure ratio engines.

Finally, some P_V contribution occurs inside compressible boundary layers with nonzero pressure gradients, where both $p - p_{\infty} \neq 0$ and frictional heating produce $\nabla \cdot \mathbf{V} \neq 0$. This contribution can be quantified via a small correction to Φ_{surf} , amounting to no more than a few percent in the overall power balance for typical transonic flows [20,25]. Furthermore, the effect would impact the BLI and non-BLI configurations nearly equally, and so the relative BLI benefit would be essentially unaffected, further supporting the applicability of the present experiments to full scale.

VI. Conclusions

The aerodynamic benefit of boundary layer ingestion was quantified via a direct back-to-back comparison of non-BLI and BLI propulsor installations on the D8 aircraft in 1:11-scale, low-speed powered model wind-tunnel tests conducted in the NASA Langley 14- by 22-foot subsonic tunnel. Using the power balance framework and the mechanical flow power as the performance metric allows for the measurement of the BLI benefit as an aircraft configuration property independently of propulsor-specific characteristics.

The experimental measurements demonstrate an aerodynamic BLI benefit of 8.6% in mechanical flow power required at the simulated cruise condition when the same propulsors are used on both configurations. This benefit level is specific to the D8, for which roughly 13% of the total airframe kinetic energy defect (or surface viscous dissipation) is ingested by the integrated propulsors. Configurations with higher ingestion will have correspondingly larger benefits.

The experiments 1) were carried out with a large model and boundary layer trips to create turbulent flow on all surfaces, 2) had nondimensional fan disk loadings and propulsive efficiencies representative of a full-size aircraft while force coefficients at cruise were matched, and 3) evaluated the BLI benefit as aerodynamic and propulsive-efficiency gains through mechanical flow power. These attributes enable the results in the present work to be general in nature, scalable, and thus provide realistic estimates of the benefits achievable with BLI for transport aircraft.

The aerodynamic benefit quantified here is only a fraction of the fuel savings that could be achieved via the use of BLI on an actual aircraft. Once the lower power requirements are taken into account and the aircraft is reoptimized with a smaller and lighter propulsor, secondary effects (linked to the reduction in engine and nacelle weights, decrease in vertical tail size and weight from reduced spacing between engines, and other compounding effects) lead to an estimated system-level BLI benefit of close to 19% [12].

Appendix A: Data Postprocessing

A.1. Correction to Specified C_L

A typical data run was started by fixing the tunnel speed and model angle of attack with the propulsors idle at a wheel speed of 5250 rpm, and then the propulsor power was varied across its full range. This power sweep produced small α , C_L , and C_m changes during the run, due to the lift-producing changes in the flow around the nacelles, as well as to the reduced pressure on the top aft fuselage of the BLI configuration. Average changes in α of 0.005 deg for the non-BLI configuration and of 0.035 deg for the BLI configuration were observed for the full-range of power change, from 5250 to 14,000 rpm wheel speed.

The measured streamwise force coefficient \tilde{C}_X is corrected to account for the corresponding change in lift needed to bring it to its desired value of $C_L = 0.64$. This is done by replacing the measured force coefficient with its corrected value

$$C_X = \tilde{C}_X + \Delta C_X \quad (\text{A1})$$

where

$$\Delta C_X = \frac{\partial C_X / \partial \alpha}{\partial C_L / \partial \alpha} (C_{L_{\text{spec}}} - \tilde{C}_L) \quad (\text{A2})$$

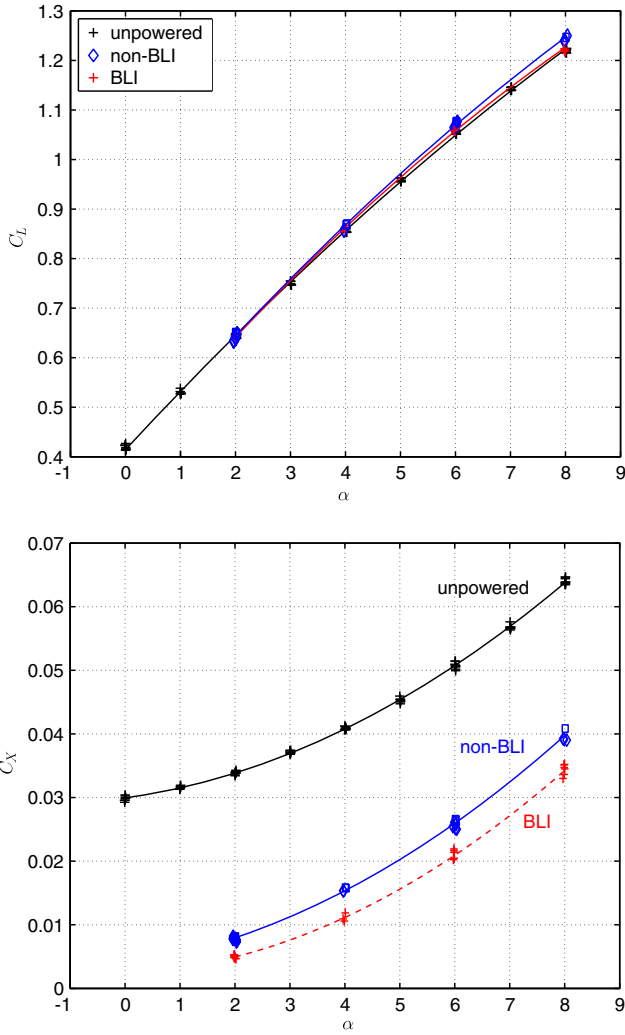


Fig. A1 Coefficients of (top) lift and (bottom) net streamwise force versus angle of attack for the three configurations with data from both tunnel test campaigns: (symbols) individual measurements and (lines) curve fits. Data for the BLI and non-BLI configurations are at $U_{\text{tip}}/V_\infty = 2.55$.

is the change that would result from the α adjustment needed to reach the desired $C_{L_{\text{spec}}} = 0.64$ value from the measured \tilde{C}_L .

The slopes $\partial C_X / \partial \alpha \approx 0.2 \text{ rad}^{-1}$ and $\partial C_L / \partial \alpha \approx 6.8 \text{ rad}^{-1}$ at 2 deg are obtained from the unpowered configuration measurements shown in Fig. A1. At cruise, the resulting ΔC_X corrections for the non-BLI and BLI configurations are typically around -1×10^{-4} and 6×10^{-4} , respectively, and are comparable or smaller than the streamwise force measurement uncertainty. Corrections due to changes in C_m are discussed Sec. V.B.

Also shown in Fig. A1 are the measured lift and streamwise force coefficients versus angle of attack for the powered configurations at a fixed wheel speed of $U_{\text{tip}}/V_\infty = 2.55$ that is close to the cruise point. The slightly higher lift of the non-BLI configuration at large angles of attack, attributed to the added lift of the non-BLI podded nacelles, is not a factor at $\alpha = 2$ deg where the correction is applied. The streamwise force coefficient curve is shifted down when power is applied, but the curve shape and slopes are largely unaffected, showing that the presence of the BLI propulsors does not appreciably affect the airframe's aerodynamic behavior with angle of attack.

A.2. Curve Fits to Data Points

Curve fits for C_X versus C_{P_K} for each configuration are constructed based on second-order polynomials using a least-squares fit through the measured points that have a C_X value between -0.026 and $+0.026$ (or, correspondingly, a C_{P_K} value between 0.01 and 0.09).

The range over which the data are fit is restricted to obtain a more accurate representation near the cruise point of $C_X = 0$. The curve-fit polynomials for the non-BLI and BLI configurations are taken to be the $C_{P_K}(C_X)$ curves measured experimentally and constitute a concrete measure of the aerodynamic performance with and without BLI.

The BLI benefit, or power-saving coefficient, for the measured data at the simulated cruise point is obtained from definition (8) and the C_{P_K} polynomial curve fits evaluated at $C_X = 0$, namely,

$$\text{PSC} = \frac{C'_{P_K}(C'_X = 0) - C_{P_K}(C_X = 0)}{C'_{P_K}(C'_X = 0)} \quad (\text{A3})$$

A.3. Confidence Intervals

At each condition, a minimum of 10 repeat runs is taken, with each set represented by a cluster of points in a C_X versus C_{P_K} plot, and the scatter of the cluster a measure of the experimental repeatability. A run is a set of data points taken at fixed nominal V_∞ and α , whereas the power level is varied via Ω . A total of 343 runs were recorded during the first test campaign of 2013 and 444 runs during the second campaign of 2014. For the non-BLI configuration, 15 and 12 runs were taken at $Re_c = 0.57 \times 10^6$ and $Re_c = 0.68 \times 10^6$, respectively. For the BLI configuration, 17 and 16 runs were taken at 0.57×10^6 and at 0.68×10^6 Reynolds numbers, respectively.

The 95% confidence intervals are calculated for the C_{P_K} data of the repeat runs using regression statistical analysis following the procedure used by Wahls et al. [31], as a way of quantifying the repeatability of the mean. The resulting confidence intervals for each configuration $\text{CI}_{\text{non-BLI}}$ and CI_{BLI} are propagated to the power saving coefficient of relation (A3) to obtain the confidence interval for the BLI benefit

$$\text{CI}_{\text{PSC}} = \sqrt{\frac{1}{C'_{P_K}} \left[\left(\frac{C_{P_K}}{C'_{P_K}} \right)^2 \text{CI}_{\text{non-BLI}}^2 + \text{CI}_{\text{BLI}}^2 \right]} \quad (\text{A4})$$

where all quantities are taken at $C_X = C'_X = 0$.

Appendix B: Uncertainty Analysis

In this section, the experimental uncertainty is quantified by applying the procedures in [31,33] to the data obtained with the indirect method during both wind-tunnel test campaigns. Additional details are given in [21]. The uncertainty in the BLI benefit PSC is found to be $\pm 1.8\%$. This is to be contrasted with the confidence interval of 0.3%, which is a measure of repeatability but does not account for instrument errors.

B.1. Methodology

The total error or uncertainty in a quantity x , denoted by U_x , is composed of two parts: bias errors and precision (random) errors. Bias errors were minimized using systematic instrument taring and zeroing, pressure sensor monitoring, and load checks. Furthermore, the configurations share a majority of the hardware and therefore are subject to most of the same biases, making the relative measure of BLI benefit insensitive to these types of errors. Bias errors are thus neglected.

Two alternative estimates of precision error P_x are considered when possible. The value of the instrumentation precision error I_x is either specified by the manufacturer or estimated from the instrument calibration. The repeatability error R_x is determined by performing multiple measurements of a variable at a given condition and different times (including the year between the two campaigns), and quantified by the 95% confidence interval on the mean (i.e., $R_x = \text{CI}_x$).

In all cases, R_x is found to be significantly smaller than I_x , indicating that manufacturer-quoted precision of the instrumentation is overly conservative. The uncertainty on any independent variable is therefore taken to be

$$U_x \simeq P_x = \min(I_x, R_x) \quad (\text{B1})$$

where I_x is chosen if R_x is not available. The uncertainty of dependent variables is then evaluated by standard error propagation.

B.2. Freestream Condition Uncertainty

The uncertainty in tunnel operating conditions is obtained from the precision of the tunnel instrumentation and is given in Table B1. All variables of interest are nondimensional and are computed from quantities that are measured and logged simultaneously. Hence, if the set tunnel condition differs from its intended value, the corresponding data point is only shifted a corresponding small amount along the C_X versus C_{P_K} curve, which itself is unchanged. Therefore, only instrumentation errors on the precision in wind-tunnel conditions are considered.

B.3. Force Measurement Uncertainty

The force balance and the accelerometer used to measure the angle of attack were provided and calibrated by NASA Langley before each tunnel test campaign. The uncertainty terms due to the imprecision in α are more than an order-of-magnitude smaller than those due to the force balance uncertainty, and the contribution of the precision in angle of attack to precision in resultant forces can be neglected.

The instrument precision for the force balance and the precision in tunnel conditions set the instrument precision in streamwise force coefficient I_{C_X} and in lift coefficient I_{C_L} , as given in Table B2. The repeatability of the force measurements R_{C_X} and R_{C_L} , given by the confidence intervals on multiple measurements at nominally constant conditions, are also given.

B.4. Electrical Power Uncertainty

The instrument precision on electrical power given in Table B2 is found from error propagation of voltage and current precisions, with the major contributor being the 1% precision error in the current monitor of the power supply. The repeatability is roughly 10 times smaller than the instrument precision.

B.5. Mechanical Flow Power Uncertainty (from the Indirect Method)

The mechanical flow power is computed as $C_{P_K} = \eta_o C_{P_E}$. Its instrument precision is

$$\frac{I_{C_{P_K}}}{C_{P_K}} = \sqrt{\left(\frac{I_{\eta_o}}{\eta_o}\right)_{\text{MIT}}^2 + \left(\frac{I_{C_{P_E}}}{C_{P_E}}\right)_{\text{LaRC}}^2} \quad (\text{B2})$$

in which the subscripts MIT and LaRC indicate where each of the quantities were measured, and an analogous relation can be written for the repeatability. The relative instrument precision for the overall efficiency is $I_{\eta_o}/\eta_o \approx 0.012$ over the range of operating conditions with a typical efficiency value of $\eta_o \approx 0.65$ [28], giving the results of Table B2. The error in η_o dominates the precision in C_{P_K} , and the rounded-off values are the same at both tunnel speeds and similar for BLI and non-BLI.

B.6. Uncertainty in Power at Cruise (from the Indirect Method)

In determining the uncertainty in power coefficient at simulated cruise, the uncertainty in the setting of $C_X = 0$ needs to be included. The equation for the propagated instrument precision at simulated cruise is

$$\frac{I_{C_{P_K}|C_X=0}}{C_{P_K}} = \sqrt{\left(\frac{I_{C_{P_K}}}{C_{P_K}}\right)^2 + \left(\frac{I_{C_X}}{C_X} \frac{dC_{P_K}}{dC_X}\right)_{C_X=0}^2}$$

with a similar equation for

$$R_{C_{P_K}|C_X=0}$$

The second term under the square root accounts for uncertainty in the streamwise force coefficient. The derivative estimated from the C_{P_K} versus C_X plot is

Table B1 Instrumentation precision in measured wind-tunnel conditions

Re_c	0.57×10^6	0.68×10^6
I_{q_∞}/q_∞	0.0013	0.0009
I_{V_∞}/V_∞	0.0008	0.0006
$I_{(qV)_\infty}/(qV)_\infty$	0.0020	0.0014

Table B2 Instrument precision and repeatability at $Re_c = 0.68 \times 10^6$

Configuration	Non-BLI	BLI
I_{C_X}	0.00047	
R_{C_X}	0.00034	
I_{C_L}	0.0016	
R_{C_L}	0.0028	
$I_{C_{P_E}}/C_{P_E}$	0.0121	Same as for non-BLI
$R_{C_{P_E}}/C_{P_E}$	0.0019	
I_{η_o}/η_o	0.0120	
R_{η_o}/η_o	0.0070	
$I_{C_{P_K}}/C_{P_K}$	0.0156	0.0157
$R_{C_{P_K}}/C_{P_K}$	0.0073	0.0072
$I_{C_{P_K} C_X=0}/C_{P_K}$	0.0217	0.0228
$R_{C_{P_K} C_X=0}/C_{P_K}$	0.0131	0.0140

Table B3 Instrument precision and repeatability in BLI benefit at cruise

Reynolds number	Re_c	0.57×10^6	0.68×10^6
Instrument precision	I_{PSC_0}	3.65%	2.94%
Repeatability	R_{PSC_0}	1.70%	1.78%
Uncertainty in BLI benefit = $\max(R_{PSC_0})$		1.8%	

$$\left. \frac{dC_{P_K}}{dC_X} \right|_{C_X=0} \simeq 1.6$$

giving the values in Table B2.

B.7. BLI Benefit Uncertainty (from the Indirect Method)

The uncertainty in the aerodynamic BLI benefit at cruise PSC_0 depends on the precision in the mechanical flow power coefficient for both BLI and non-BLI configurations, which combine to give

$$I_{PSC_0} = \frac{C_{P_K BLI}}{C_{P_K non-BLI}} \sqrt{\left(\frac{I_{C_{P_K}|C_X=0}}{C_{P_K}} \right)_{non-BLI}^2 + \left(\frac{I_{C_{P_K}|C_X=0}}{C_{P_K}} \right)_{BLI}^2}$$

A similar equation gives the repeatability R_{PSC_0} , with the results presented in Table B3. Because the instrument precisions were found to be overly conservative, the repeatability value is more representative of the actual uncertainty in the measured BLI benefit. The higher of the R_{PSC_0} values at 0.57 and 0.68 million Reynolds numbers is used as the uncertainty, namely 1.8%.

B.8. Summary of Uncertainty Analysis

Repeat runs at the NASA Langley 14- by 22-foot subsonic tunnel were spread throughout the 4–6 weeks of tests in each of the two campaigns, separated by a number of model changes during a single campaign and a delay of one year between each campaign. The repeatability is found to be consistently and significantly smaller than the instrument precision values, and therefore the repeatability of the experimental data is a more appropriate measure of the uncertainty. The measured cruise BLI benefit can be quoted as $PSC = (8.6 \pm 1.8)\%$, meaning that the uncertainty fraction is $\pm 1.8/8.6\% = \pm 0.21$.

Acknowledgments

This work was supported by the NASA Fundamental Aeronautics Program, Fixed Wing Project, through Cooperative Agreement Number NNX11AB35A. We emphasize that the authors are only part of the extended collaboration that is an enabling feature of this project. In this regard, we are pleased to acknowledge contributions from the rest of the Massachusetts Institute of Technology (MIT) N + 3 team: this includes Elise van Dam from Delft University of Technology, the 13 MIT undergraduate students who completed internships with the project, and our partners at Aurora Flight Sciences and Pratt and Whitney, especially the insights on propulsion-airframe integration contributed by Wes Lord. From NASA Langley, we thank Scott Anders for his guidance and valuable suggestions. We benefited enormously from the expertise and enthusiasm of the staff of the NASA Langley 14- by 22-foot subsonic tunnel, in particular Jim Byrd and Les Yeh who served as test engineers during the two experimental campaigns. We would also like to acknowledge Shishir Pandya from NASA Ames for his work on numerical simulations. We are most appreciative of the strong interest, support, and useful input contributed by the NASA Fixed Wing Project management, especially Rubén del Rosario, Richard Wahls, and Kim Pham. We thank Harold Youngren of Aerocraft, Inc. who was instrumental in performing the computational fluid dynamics studies during the model design phase. We also wish to thank the many people who offered technical feedback, in particular,

N. Cumpsty, Y. Dong, A. Epstein, E. Gallagher, R. Liebeck, A. Murphy, J. Sabnis, and G. Tillman.

References

- [1] *FAA Aerospace Forecast Fiscal Years 2014–2034*, Federal Aviation Admin., Washington, D.C., 2014, p. 42.
- [2] *Boeing Current Market Outlook 2014*, Boeing Commercial Airplanes Market Analysis, Boeing, 2014.
- [3] *Global Market Forecast, Flying on Demand 2014–2033*, AIRBUS S.A. S. 31707, Airbus, 2014, p. 10.
- [4] “ICAO Resolution 37-19,” *37th ICAO Assembly*, ICAO, Sept.–Oct. 2010.
- [5] “The Right Flightpath to Reduce Aviation Emissions,” Position Paper, Air Transportation Action Group, United Nations Framework Convention on Climate Change Climate Talks, Geneva, Nov. 2010.
- [6] Liebeck, R. H., “Design of the Blended Wing Body Subsonic Transport,” *Journal of Aircraft*, Vol. 41, No. 1, 2004, pp. 10–25. doi:10.2514/1.9084
- [7] Kawai, R., Friedman, D., and Serrano, L., “Blended Wing Body (BWB) Boundary Layer Ingestion (BLI) Inlet Configuration and System Studies,” NASA CR-2006-214534, 2006.
- [8] Felder, J. L., Kim, H. D., Brown, G. V., and Chu, J., “An Examination of the Effect of Boundary Layer Ingestion on Turboelectric Distributed Propulsion Systems,” *AIAA SciTech, 49th Aerospace Sciences Meeting*, AIAA Paper 2011-0300, Jan. 2011. doi:10.2514/6.2011-300
- [9] Wick, A. T., Hooker, J. R., Hardin, C. J., and Zeune, C. H., “Integrated Aerodynamic Benefits of Distributed Propulsion,” *AIAA SciTech, 53rd Aerospace Sciences Meeting*, AIAA Paper 2015-1500, Jan. 2015. doi:10.2514/6.2015-1500
- [10] Greitzer, E. M., et al., “N + 3 Aircraft Concept Designs and Trade Studies, Final Report,” NASA CR 2010-216794, 2010.
- [11] Drela, M., “Development of the D8 Transport Configuration,” *29th AIAA Applied Aerodynamics Conference*, AIAA Paper 2011-3970, June 2011. doi:10.2514/6.2011-3970
- [12] Uranga, A., Drela, M., Greitzer, E. M., Titchener, N. A., Lieu, M. K., Siu, N. M., Huang, A. C., Gatlin, G. M., and Hannon, J. A., “Preliminary Experimental Assessment of the Boundary Layer Ingestion Benefit for the D8 Aircraft,” *AIAA SciTech, 52nd Aerospace Sciences Meeting*, AIAA Paper 2014-0906, Jan. 2014. doi:10.2514/6.2014-0906
- [13] Drela, M., “Power Balance in Aerodynamic Flows,” *AIAA Journal*, Vol. 47, No. 7, 2009, pp. 1761–1771. doi:10.2514/1.42409
- [14] Betz, A., “Interference Between Propeller and Vehicle: The Ducted Propeller,” *Introduction to the Theory of Flow Machines*, Pergamon, New York, 1966, pp. 215–217.
- [15] Smith, L., “Wake Ingestion Propulsion Benefit,” *Journal of Propulsion and Power*, Vol. 9, No. 1, 1993, pp. 74–82. doi:10.2514/3.11487
- [16] Atinault, O., Carrier, G., Grenon, R., Verbecke, C., and Viscat, P., “Numerical and Experimental Aerodynamic Investigations of Boundary Layer Ingestion for Improving Propulsion Efficiency of Future Air Transport,” *AIAA 31st Fluid Dynamics Conference*, AIAA Paper 2013-2406, June 2013. doi:10.2514/6.2013-2406
- [17] Arend, D., Tillman, G., and O’Brien, W., “Generation After Next Propulsor Research: Robust Design for Embedded Engine Systems,” *48th AIAA/ASME/SAE/ASEE Joint Propulsion Conference*, AIAA Paper 2012-4041, July–Aug. 2012. doi:10.2514/6.2012-4041
- [18] Florea, R., Voytovych, D., Tillman, G., Stucky, M., Shabbir, A., and Sharma, O., “Aerodynamic Analysis of a Boundary-Layer-Ingesting Distortion-Tolerant Fan,” *ASME Turbo Expo 2013*, American Soc. of Mechanical Engineers Paper GT2013-94656, June 2013. doi:10.1115/GT2013-94656

- [19] Hall, D. K., Greiter, E. M., and Tan, C. S., "Analysis of Fan Stage Design Attributes for Boundary Layer Ingestion," *Journal of Turbomachinery*, Vol. 139, No. 7, 2017, Paper 071012.
doi:10.1115/1.4035631
- [20] Hall, D. K., Huang, A. C., Uranga, A., Greitzer, E. M., Drela, M., and Sato, S., "Boundary Layer Ingestion Propulsion Benefit for Transport Aircraft," *Journal of Propulsion and Power*, May 2017.
doi:10.2514/1.B36321
- [21] Uranga, A., et al., "Aircraft and Technology Concepts for an N + 3 Subsonic Transport, Phase 2 Final Report," NASA CR (to be published).
- [22] Lord, W., Suciu, G., Hasel, K., and Chandler, J., "Engine Architecture for High Efficiency at Small Core Size," *AIAA SciTech, 53rd Aerospace Sciences Meeting*, AIAA Paper 2015-0071, Jan. 2014.
doi:10.2514/6.2015-0071
- [23] Kawai, R., Friedman, D., and Serrano, L., "Blended Wing Body (BWB) Boundary Layer Ingestion (BLI) Inlet Configuration and System Studies," NASA CR 2006-214534, 2006.
- [24] Hardin, L. W., Tillman, G., Sharma, O. P., Berton, J., and Arend, D. J., "Aircraft System Study of Boundary Layer Ingesting Propulsion," *48th AIAA/ASME/SAE/ASEE Joint Propulsion Conference*, AIAA Paper 2012-3993, July–Aug. 2012.
doi:10.2514/6.2012-3993
- [25] Sato, S., "The Power Balance Method for Aerodynamic Performance Assessment," Ph.D. Thesis, Massachusetts Inst. of Technology, Cambridge, MA, June 2012, <http://hdl.handle.net/1721.1/75837> [retrieved 2 May 2017].
- [26] Lieu, M. K., "Quantification of the Boundary Layer Ingestion Benefit for the D8-Series Aircraft Using a Pressure Rake System," M.S. Thesis, Massachusetts Inst. of Technology, Cambridge, MA, Feb. 2015, <http://hdl.handle.net/1721.1/97264> [retrieved 2 May 2017].
- [27] Lieu, M., Uranga, A., Drela, M., and Greitzer, E., "Rapid Flow Surveys via Rotating Rake System and Use in Powered Wind Tunnel Models," *AIAA Aviation, 30th AIAA Aerodynamic Measurement Technology and Ground Testing Conference*, AIAA Paper 2014-2801, June 2014.
- [28] Siu, N., "Evaluation of Propulsor Aerodynamic Performance for Powered Aircraft Wind Tunnel Experiments," M.S. Thesis, Massachusetts Inst. of Technology, Cambridge, MA, Feb. 2015, <http://hdl.handle.net/1721.1/97265> [retrieved 2 May 2017].
- [29] Siu, N., Titchener, N., Casses, C., Huang, A., Uranga, A., Drela, M., and Greitzer, E., "Evaluating Propulsor Mechanical Flow Power in Powered Aircraft Wind Tunnel Experiments," *AIAA Aviation, 32nd AIAA Applied Aerodynamic Conference*, AIAA Paper 2014-25661, June 2014.
doi:10.2514/6.2014-2566
- [30] Casses, C., "Aerodynamic Benefits of Boundary Layer Ingestion for the D8 Double-Bubble Aircraft," M.S. Thesis, Massachusetts Inst. of Technology, Cambridge, MA, Sept. 2015, <http://hdl.handle.net/1721.1/101494> [retrieved 2 May 2017].
- [31] Wahls, R. A., Adcock, J. B., Witkowski, D. P., and Wright, F. L., "A Longitudinal Aerodynamic Data Repeatability Study for a Commercial Transport Model Test in the National Transonic Facility," NASA TP 3522, 1995.
- [32] Drela, M., "XFOIL: An Analysis and Design System for Low Reynolds Number Airfoils," edited by T. Mueller, *Low Reynolds Number Aerodynamics*, Lecture Notes in Engineering, Vol. 54, Springer–Verlag, New York, 1989.
- [33] "Assessment of Experimental Uncertainty with Applications to Wind Tunnel Testing," AIAA Standards S-071A-1999, Reston, VA, 1999.

I. Gursul
Associate Editor